Progress In Electromagnetics Research, Vol. 140, 105–129, 2013

ARTIFICIAL MAGNETIC MATERIALS SYNTHESIS WITH GENERIC METALLIC BROKEN LOOPS

Ali Kabiri[1] and Omar M. Ramahi[2, *]

[1]School of Engineering and Applied Science, Harvard University, Cambridge, MA, USA

[2]Department of Electrical and Computer Engineering, University of Waterloo, Waterloo, ON, Canada

Abstract—We propose a methodic approach to design Artificial Magnetic Materials (AMM) with desired magnetic properties. The design procedure is defined based on a novel formulation for characterizing AMMs. The employed formulation expresses the effective permeability and the magnetic loss tangent (MLT) in terms of the geometrical and physical parameters of the inclusions. The method comprised four steps. In the first step, the feasibility of the design is checked through a set of constraints. The second and third steps provide an iterative procedure to capture the desired magnetic properties. Finally, the geometrical elements, i.e., the area and perimeter of inclusions, are calculated. The technique is applied to design of an AMM structure based on Rose curve resonators. The design based on the proposed methodology is verified by the numerical simulation of the AMM.

1. INTRODUCTION

In recent years, there has been an increasing interest in developing, designing and fabricating artificial electromagnetic materials (or metamaterials) with properties not found in nature. Among artificial structures, those that disclose magnetic behaviors have been received more attention due to not only providing positive or even negative permeability at radio frequencies, but because of important potential applications.

Pendry et al. [1] proposed artificial magnetic materials (AMM) composed of electrically small metallic broken-looped resonators

Received 15 February 2013, Accepted 18 April 2013, Scheduled 27 May 2013

* Corresponding author: Omar M. Ramahi (oramahi@uwaterloo.ca).

referred to as split-ring resonators (SRR). Since then, numerous inclusions having various geometrical configurations have been proposed in the literature to achieve enhanced magnetic properties. A modified SRR (m-SRR), or broadside coupled SRR (bc-SRR) was introduced in [2]. In [3], a new configuration, the metasolenoid was proposed with the potential to provide higher permeability compared to SRR and m-SRR configurations. In [4], the n-turn Spiral Resonator (n-SR) configuration was introduced. Figure 1 shows a sample set of inclusions presented in the literature. These inclusions have been employed as a building block of metamaterial slabs.

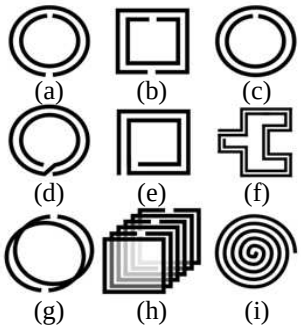

Figure 1. Different inclusions used to implement artificial magnetic materials. (a) Double split-ring resonators (d-SRR). (b) Double split square resonators (d-SSR). (c) Singly split-ring resonator (s-SRR). (d) Two-turn (circular) spiral resonator (2c-SR), (e) Two-turn (rectangular) spiral resonator (2r-SR). (f) Hilbert-fractal resonator. (g) Modified ring resonator (m-SRR). (h) Metasolenoid. (i) Cross section of a Swiss roll (SR).

The electromagnetic properties of metamaterials have generated new applications. These growing applications are using metamaterial slabs as a probe for the near-field sensing [5], as a substrate or a superstrate for enhancing low-profile antenna performance [6], as a perfect lens for microwave imaging [7], as microwave shields or absorbers [8] and even as bio-sensors for medical applications [9].

A number of analytical models were developed to characterize the behavior of an AMM with a specific inclusions' configuration [1, 3, 4]. When AMMs are described by the continuum-medium approach, the inclusion and unit cell size of the composite structure should be much smaller than the wavelength in the free space. Thus, analytical models employing localized field theories such as the effective medium theory (EMT) and homogenization theories (HT) can be used to calculate the

magnetic properties of composite media [10]. Due to the small feature size of the inclusions in composite media and the small skin depth, the magnetic response of such media can be interpreted in terms of the geometric parameters of the inclusions rather than electromagnetic properties of the metals [11]. From this point of view, circuit-based model of the AMMs are justified to describe the behavior of the structures in terms of electrical lumped elements (i.e., R, L and C).

In 2002, Marques et al. presented a quasi-static study of the SRR by proposing a circuit model for the capacitive behavior of the inclusions [2]. Two years later, Sauviac et al. and Shamonin et al. proposed more accurate models for SRR inclusions [12, 13]. Ikonen et al. offered a generalized equivalent-circuit model which mimics the experimental permeability function [14]. In [15] a general circuit model describing the effect of the spatial and temporal dispersion in AMMs is presented. The spatial dispersion is effective in smaller wavelength (higher frequency) limits. The work in [11] provided a simple but general formulation for characterizing magnetic behavior of AMMs based on two newly defined parameters–physical and geometrical parameters. Geometrical factors are area, perimeter and curvature function of an inclusion. Physical factors are structural, fabrication and electrical parameters of the inclusions and the medium. The very advantage of such a description is that it allows for the parametric study of AMMs as well as design guidelines. The new formulations reveal that the geometrical factor plays a key role in characterizing the real part of the effective permeability and the physical factor contributes to the magnetic loss tangent (MLT) of AMMs. In addition, the work provided some fundamental limitations on the behavior of AMMs.

The main challenge in developing a circuit model is to precisely predict the behavior of the AMM at the vicinity of the resonance frequency and beyond. Far enough from the resonance frequency, the challenge is not severe as all circuit models give identical response and converge to the same value.

The present work aims to establish a design methodology and novel topologies for AMMs. To the best of our knowledge, there is no recipe for synthesizing AMMs to meet specific applications. However, simulating and modeling of AMM structures have been addressed extensively in the literature. Many analyses used electromagnetic full-wave simulations to study the magnetic behavior of AMMs [16] and provide a desirable specification. Our analysis and strategy of design is general and can be applied to any choice of circuit model. As long as a circuit model is suitable for describing a composite medium it can be adopted by the methodology presented here. Since we are

interested to provide a solution for design of an AMM (enhanced positive permeability) with low loss and less dispersion, we adopt a circuit model which is based on a solenoidal approximation and on the area and perimeter of the inclusions.

In this work, we propose an iterative approach to synthesize the desired criteria by engineering the geometry of the inclusions. We introduce a methodology to characterize the length and perimeter of the inclusions of an AMM meeting desired criteria, and we examine the proposed methodology in design of a specific design scenario using Rose curve resonators. Full-wave numerical simulations are provided for verification of effectiveness of the design.

2. BACKGROUND

In an artificial medium impinged with an external monochromatic magnetic field $\mathbf{H}_{ext}$, the effective magnetic susceptibility represents the degree of magnetization of the medium in response to an applied magnetic field, defined as:

$$\chi_m = \frac{M_{med}}{H_{ave}} \tag{1}$$

where H_{ave}, the magnitude of an averaged (macroscopic) magnetic field $\mathbf{H}_{ave}$ inside the medium, is defined by averaging magnetic field along the sides of the unit cell, and M_{med} is the magnitude of the magnetization vector of the medium. Magnetization is defined as the magnetic moment per volume. When the magnetic dipole moments are in phase with the averaged magnetic field, the effective magnetic susceptibility become larger than zero (correspondingly, the effective permeability become larger than unity) causing the medium to be magnetized. Note that in some special cases such as placing an AMM inside a long solenoid, $\mathbf{H}_{ext} = \mathbf{H}_{ave}$.

An expression for the magnetic susceptibility is formulated by considering an AMM with a general inclusion's shape. Figure 2(a) shows a two-turn split-ring resonator with an arbitrary trace geometry denoted by $\Gamma(s, l)$. Γ is characterized by s and l, the area and the perimeter of the inclusion, respectively. Figure 2(b) and Figure 2(c) show an edge-coupled and a broadside-coupled ring resonator, respectively [17]. The unit sample in Figure 2(a) has a height of δz width of δx and depth of δy. The area of the cell is $A = \delta x \delta z$ and its volume is $V = A\delta y = \delta x \delta y \delta z$. Arrays can be arranged in a periodic or aperiodic fashion, spread along the x, y and z axes to produce the AMM. In this work, we consider a periodic arrangement of the resonators.

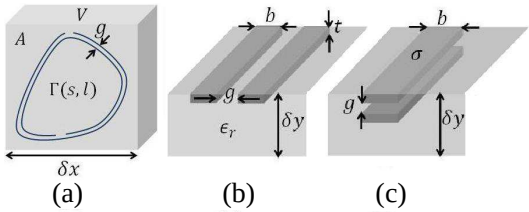

Figure 2. (a) A configuration of a unit cell of an AMM with an arbitrary shape SRR. V and A represent the volume and surface area of the unit cell. The inclusions' contour, area and perimeter are denoted by Γ, s, and l, respectively. (b) Edge-coupled inclusion. (c) Broadside-coupled inclusion.

As the inclusions were arranged in parallel planes, the AMM is essentially an anisotropic structure, and provides the susceptibility and magnetic moment vectors only in the direction perpendicular to the inclusion surface (here, in the y direction). Hence, the magnetic susceptibility $\bar{\bar{\chi}}_{m\text{eff}}$ describing the medium is a tensor. Also, the susceptibility in the x and z directions is directions is equal to that of the host media which is zero for nonmagnetic host medium. Therefore, the artificial magnetic material will be anisotropic with susceptibility tensor of

$$\bar{\bar{\chi}}_{m\text{eff}} = \begin{pmatrix} \chi_{mr} & 0 & 0 \\ 0 & \chi_{m\text{eff}} & 0 \\ 0 & 0 & \chi_{mr} \end{pmatrix} \tag{2}$$

where χ_r is the susceptibility of the host medium.

To achieve an isotropic AMM the same inclusions can be rearranged in parallel planes intersecting the plane of inclusions (in the x and z directions). Therefore, a unit cell is designed as a cubit cell with inclusions attached on the three walls, i.e., in xy, xz and yz planes [18]. In [19], it was shown that among various orientations of the rings, for an isotropic response, the rings can only intersect along symmetric points.

A precise consideration of the behavior of the inclusions shows that the particle behaves like a magnetic dipole and an electric dipole in response to an external magnetic. This behavior makes the structure bi-anisotropic. The bianisotropy effect is reduced when the operation frequency is not close to the resonance frequency, and goes to a minimum for inclusions with broadside coupling. In this work, we only address the magnetic behavior of the structures [2].

The magnetic dipole moment of inclusions can be stated as:

$$\vec{m}_{incl} = nsI\hat{y} \tag{3}$$

where I is the induced current, n is the number of wire turns that carries the induced current [3]. The magnetic susceptibility can be written as:

$$\chi_m = \frac{nsI}{VH_{ave}} \tag{4}$$

The effective magnetic susceptibility of the composite follows the following functional form in the quasi-static regime, and is expressed as [1, 16, 14]:

$$\chi_m(\omega) = \frac{K\omega^2}{\omega_0^2 - \omega^2 + j\gamma\omega} \tag{5}$$

where K, $(0 < K < 1)$, is the amplitude factor, ω_0 is the resonant frequency of the inclusions, defined to be the frequency at which χ_m is purely imaginary, and γ is the loss factor. Figure 3 shows the real and imaginary part of the effective magnetic susceptibility function for a typical AMM introduced by (5).

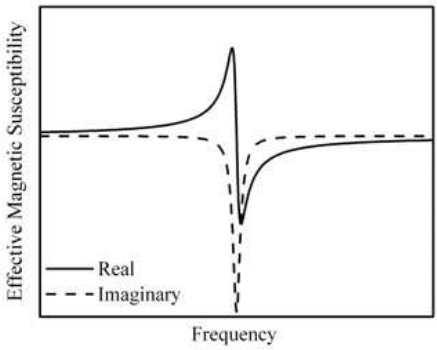

Figure 3. typical response of an artificial magnetic material. The graph shows the magnetic susceptibility as a function of frequency. Note no specific frequency scale depicted.

The model described in (5) provides valid responses at low frequencies and in the vicinity of the resonance frequency. However, in the limit as $\omega \to \infty$, $\chi_m \to -K$, which contradicts the expected physical behavior of χ_m. At extremely high frequencies, because of the electron's inertia, the materials cannot be magnetized, implying $\chi_m \to 0$, and hence, the model breaks down [20].

Note that the operational frequency falls in a range of frequency where the resonance frequency is a fixed design property. Therefore, the parameters which are dependent on the operational frequency

cannot uniquely be designed for desired application. In other words, the value of parameters such as γ will vary with operational frequency leading to a complicated or unpredictable model behavior prior to design. To simplify the model and to facilitate the design procedure, the frequency needs to be extracted from the parameters and be expressed explicitly in the model as will be shown below.

In [11], an alternative formula to (5) was introduced based on defined geometrical and physical parameters. χ_m is expressed in terms of the physical factor P and geometrical factor F as:

$$\chi_m(\Omega; F, P) = \chi_0(\Omega)(1 + j\sqrt{\xi(\Omega)})^{-1} \tag{6}$$

where Ω is the normalized frequency ($\Omega = \frac{\omega}{\omega_0}$). $\chi_0(\Omega)$ is the magnetic susceptibility of lossless medium, and $\xi(\Omega)$ is the loss factor:

$$\chi_0(\Omega) = F \cdot f_1(\Omega) \tag{7}$$

$$\xi(\Omega) = \frac{P^2}{F^4} \cdot f_2(\Omega) \tag{8}$$

where

$$f_2(\Omega) = \frac{f_1^2(\Omega)}{\Omega} = \frac{\Omega^3}{(1-\Omega^2)^2} \tag{9}$$

Following [11], the geometrical factor F and the physical factor P are expressed as:

$$F = \frac{s}{A} \tag{10}$$

$$P = \mathcal{K}\omega_0^{-\frac{5}{2}} \tag{11}$$

$$\omega_0 = \frac{\mathcal{Q}}{\sqrt{sl}} \tag{12}$$

where $\mathcal{K} \equiv \mathcal{K}(A, b, g, t, \sigma, \epsilon_r, \mu_r)$ is a function of the structural and electrical properties of the inclusions and the unit cell (see Figure 2 for description of the parameters of $\mathcal{K}$), and $\mathcal{Q}$ is a function of the structural and electrical properties of the inclusions and host medium. F can also be read as the fractional area of the cell occupied by the interior of the inclusion, ranging from 0 to 1.

The advantage of the formula in (6) is that the topological properties of the inclusion's contour such as surface area and perimeter of the inclusions and the physical properties of the design appear *explicitly* in the formula as two factors. In fact, the strongest feature of the model is that inclusions with different topologies but having identical perimeter and area, result in the same values for the magnetic susceptibility and permeability.

From (5)–(8), the equivalence between (5) and (6) is established through the following equalities

$$F = K \tag{13}$$

$$P = \frac{\gamma K^2}{\sqrt{\omega\omega_0}} \tag{14}$$

Note that since γ has a linear dependence on $\sqrt{\omega}$ [14], surprisingly, F and P are *completely* independent of the operational frequency.

Using (6), the permeability can be written as:

$$\mu(\Omega; F, P) = 1 + \chi_m = 1 + \chi_0(\Omega)(1 + j\sqrt{\xi(\Omega)})^{-1} \tag{15}$$

In design of an AMM, the real effective permeability and the magnetic loss tangent (MLT) of the composite medium are basic objectives of the design. Throughout the design steps, while synthesizing the inclusions' geometry, ceteris paribus, the real permeability and magnetic loss of the engineered medium are desirably specified for a particular application. Hence, for design purposes, these two significant properties of AMMs are formulated based on geometrical and physical parameters of the medium. Using (6), the real effective permeability and the MLT are expressed respectively as:

$$\mu_{\mathrm{Re}}(\Omega) = 1 + \chi_0(1 + \xi)^{-1} \tag{16}$$

$$\tan\delta(\Omega) = -\frac{\mu_{\mathrm{Im}}(\Omega)}{\mu_{\mathrm{Re}}(\Omega)} = \chi_0\sqrt{\xi}\,(1 + \chi_0 + \xi)^{-1} \tag{17}$$

In subsequent sections, the aforementioned equations are exploited in design of AMMs meeting specific operational requirements.

3. DESIGN METHODOLOGY

In this section we introduce a design recipe for AMMs. We propose to design an AMM with specified unit cell size and effective magnetic permeability larger than unity over a range of frequencies. The resonant frequency of the inclusions can be set through the design procedure, but the permeability is designed for minimum allowable dispersion within the frequency band. Moreover, the design is desired not to exceed a certain magnetic loss tangent over a specific frequency range. The outcome of the design is the dimension of the inclusion or the geometrical and physical parameters of the medium. However, many fabrication and structural parameters cannot be varied due to fabrication and design constrains, such as the thickness of the metal of the board, the conductivity of the conductor, the permeability of the host medium, or width of the conductor's routes. Therefore, all these values will be considered as design constraints.

The procedure is summarized as follows: First step is testing the feasibility of the design. In this step, the requested values will be tested against the fundamental limitations of AMMs as discussed in [11, 21].

Next, by using the fixed and requested design parameters, and employing relations (16) and (17), a valid interval for the resonance frequency of the inclusions and subsequently for the geometrical and physical factors will be calculated. The provided intervals of parameters specify the magnetic properties of the structure within a range in which the desired values are located. In the third step, the frequency range of the resonance frequency and the geometrical and physical factors are modified to achieve a suitable tolerance for the magnetic properties of the structure. Although a very narrow range of tolerance can be obtained, it is preferable to determine the design ranges constrained by fabrication and application tolerances. Finally, by using the two calculated geometrical and physical factors, the length and area of inclusions will be derived. Figure 4 shows the main steps of the design methodology.

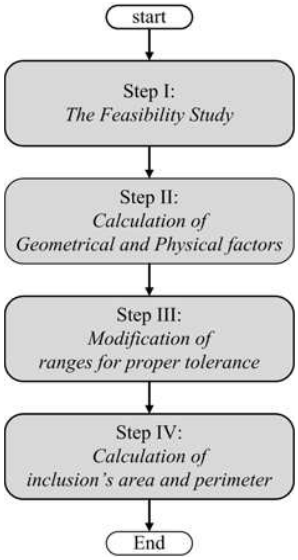

Figure 4. The flowchart shows the main steps to derive the geometrical and physical factors from which the area and perimeter of inclusions will be determined.

Note that, even though (6)–(12) are general enough to model AMMs composed of inclusion with edge and broadside coupling scheme and various topologies such as multi-filar spirals and n-broken

ring resonators, they do not model AMMs performing under non-solenoidal mechanism (such as far apart constituent arrangements), multi-resonators and other loss mechanism. Also, (6)–(12) do not model AMMs composed of non-metallic inclusions. Therefore, the design recipe is suitable for design of a specific class of AMMs. However, applying the general guidelines in Figure 4, a designer can generate a new design recipe based on another novel circuit model.

A design case study based on the adapted circuit model is considered next.

4. DESIGN CASE STUDY

In this section, the design procedure for synthesizing the inclusions' geometry of an AMM is described in details through a case study. Firstly, by considering desired operational properties for an AMM, the physical and geometrical parameters attributed to medium structure are characterized. That secondly, by using structural equations (i.e., (10)–(12)), the perimeter and area of inclusions determined. The synthesized geometrical parameters are used to propose a suitable geometry for inclusions.

Table 1 shows an example of a design request sheet. The designed structure can possibly be used as a substrate for miniaturizing a patch antenna operating at 600 MHz. Some variables such as conductivity and host medium permittivity were set. The design needs to meet a number of conditions such as μ_{Re} at a specific operational frequency of $f_{op} = 6.00 \times 10^8$ Hz is equal $9.00 \pm 5.0\%$ within the frequency range of at least 2 MHz, and MLT of less than 5.00×10^{-2}.

4.1. Step I — The Feasibility Study

First we verify if the frequency bandwidth is achievable within the specified tolerance for the permeability. From [11],

$$\frac{BW}{\omega_{op}} \leq \frac{1}{2\chi_{op}} \left(\frac{\delta\mu}{\mu_{op}} \right) \tag{18}$$

where ω_{op}, μ_{op} and χ_{op} are the operational frequency, the effective permeability and the magnetic susceptibility, respectively. BW and $\delta\mu$ represent the frequency bandwidth and the permeability deviation, respectively. (Note that the operational frequency should not be confused with the resonance frequency of the inclusion. The operational frequency basically represents a specific frequency at which certain application, say an antenna, is operating). Inequality (18) stated that the flatness of the permeability function is limited by the

Table 1. Design data sheet.

Material Specifications
Host medium: `Duroid 5880` ($\varepsilon_r = 2.2$)
Traces: `Copper` ($\sigma = 59.6 \frac{\mathrm{S}}{\mu\mathrm{m}}$)
Fabrication Technique Parameters and Design Dimensions
Trace width: $b = 200\,\mu\mathrm{m}$
Trace gap: $g = 800\,\mu\mathrm{m}$
Metal thickness: $t = 35\,\mu\mathrm{m}$
Fabrication tolerance: 0.25%
Unit cell size: $(\delta x, \delta y, \delta z) = (20.0\mathrm{mm}, 800\,\mu\mathrm{m}, 20.0\,\mathrm{mm})$
Design Request
Inclusion type: `Metasolenoid`
Operational frequency: $f_{op} = 600\,\mathrm{MHz}$
Real effective permeability: $\mu_{op} \pm \delta\mu = 9.00 \pm 5.0\%$
Bandwidth: $BW \approx 2\,\mathrm{MHz}$
Magnetic Loss Tangent (MLT): $\tan\delta < 0.050$

desired operational bandwidth. Although this relation is derived for the lossless and time-dispersive medium, it has been shown that for the lossy medium the restriction is an upper bound.

The second constraint is to find a boundary for the physical and geometrical factors by setting the maximum of the permeability function over all frequencies (see Figure 3) high enough to cover the effective permeability requirement declared in Table 1. From Table 1, the real effective permeability is $8.55 < \mu_{\mathrm{Re}} < 9.45$, as such, the maximum of the real effective permeability function should be larger than $9.45\,(\mu_{\max} > 9.45)$. From (16) it can be shown that (see Appendix A)

$$\mu_{\max} \simeq 1 - \frac{F}{8} + \frac{F^3}{2P} \tag{19}$$

Substituting the upper value of the permeability from Table 1, (19) can be rearranged as

$$P < \frac{4F^3}{67.6 + F}$$

which for $F = 1$ (F upper bound), we get $P < 0.0583$, an upper limit for P.

4.2. Step II — Calculation of the Geometrical and Physical Factors

In this step, first valid ranges for the normalized operational frequency, geometrical factor and physical factor are being calculated consecutively. Then, by considering the constraint on the maximum value of the permeability introduced in Step I, ranges are being modified for each parameter.

Solving the relation (16) and (17) simultaneously for a given value of the real effective permeability and the magnetic tangent loss, we obtain

$$\xi(\Omega_{op}) = \left[\frac{\mu_{\mathrm{Re}\,op}}{\chi_{m\,op}}\tan\delta_{op}\right]^2 \tag{20}$$

$$\chi_0(\Omega_{op}) = \chi_{m\,op}\left(1+\left[\frac{\mu_{\mathrm{Re}\,op}}{\chi_{m\,op}}\tan\delta_{op}\right]^2\right) \tag{21}$$

Substituting from Table 1 in (20) and (21), we obtain $\xi(\Omega_{op}) = 3.164\times10^{-3}$ and $\chi_0(\Omega_{op}) = 8.025$. Afterwards, ξ and χ are considered fixed parameters for the design, and Ω and P are calculated based on a valid range of F, accordingly.

By considering the definition (7) and sweeping F over the possible range of [0, 1], the normalized operational frequency falls within

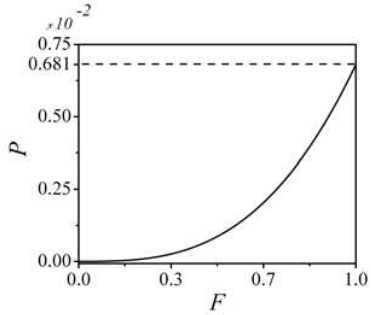

Figure 5. Any point on the curve represents a pair of (F, P) for which the design meet desired properties introduced in Table 1.

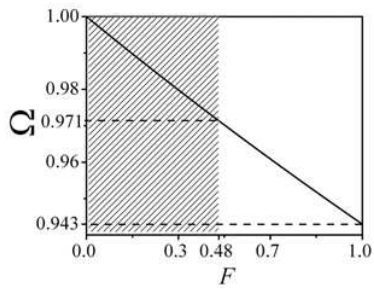

Figure 6. The graph shows the relation between the normalized frequency Ω and the geometrical factor F. The hashed area is an area which the peak of real effective permeability function goes under the requested permeability.

[0.9430, 1]. Then, by using data set of (F, Ω_{op}) obtained from (7), the physical factor P is calculated from (8), and the graph of P is plotted versus the geometrical factor F in Figure 5. The graph shows a valid range of $[0, 0.0068]$ for P. In fact, any point on the graph in Figure 5 corresponds to a possible pair of (F, P) meeting the properties promised in Table 1 except the fact that we need to choose a suitable pair for which the design works at a specific operational frequency (here; 600 MHz).

Next, the calculated ranges are modified to a smaller range by applying the inequality in (19). From Figure 5, the upper bound of P can be read as 6.806×10^{-3} which is clearly less than 0.0583 (see the example illustrated for inequality (19)). Based on the relation (19), $P = 6.806 \times 10^{-3}$ limits F from the below to 0.4875 leading to a new valid range of $[0.4875, 1]$ for F.

Figure 6 shows the normalized operational frequency plotted versus F with the banned values of F cross-hashed in the figure. The graph shows a valid range of $[0.9430, 0.9710]$ for Ω_{op}. The banned range of F has also been cross-hashed in the graph of P versus F (see Figure 7). In fact, in Figure 6 and Figure 7, the white region represent the criteria in which the maximum of the real effective permeability function goes above the requested permeability (here; 9.45).

4.3. Step III — The Resonance Frequency Calculation

In this step, the resonance frequency for the design is determined iteratively. Each iteration involves two parts; first, calculating a range for the resonance frequency and then modifying the calculated range for the geometrical and physical factors. If the iterations is successful, smaller ranges for the resonance frequency, the geometrical and physical factors are achieved. The iterations is continued so that the variations of the physical and geometrical factors over their calculated ranges are less than the fabrication tolerance indicated in the Table 1. This is due to the fact that the variation of dimensions linearly affects the geometrical and physical factors [11].

In the first part, by using the data obtained in the Step II for the physical factor P, the material specifications and fabrication characteristics provided in Table 1 and (14), an interval for the feasible resonance frequency of the realizable inclusions is calculated. Figure 8 shows the calculated resonance frequency as a function of P and F. Also, the improper values of F has been cross-hashed in Figure 8. (Note that due to the fact that F and P are not linearly dependant, the scale for the F axes remained linear, however, the P axes is not linear. Therefore, each value on the P axes pertains to its F correspondent pair).

From Figure 6, It can be seen that $0.9430 < \Omega_{op} < 0.9710$ which corresponds to $617.9\,\text{MHz} < f_{res} < 636.3\,\text{MHz}$ ($617.9\,\text{MHz} = \frac{f_{op}}{0.9710}$). The calculated range for the resonance frequency has been marked in Figure 8 with two horizontal dashed-lines.

In the second part, by using (11) and the calculated range of the resonance frequency, the range for the physical factor is modified. Also, as the physical and geometrical factors are coupled through relation (8) (also, see Figure 7), a range for the geometrical factor is modified. The vertical dashed-lines in Figure 8 shows the newly modified ranges of the physical and geometrical factors. From Figure 8, the ranges of F and P can be read as $0.4916 < F < 0.5038$ and $8.209 \times 10^{-4} < P < 8.833 \times 10^{-4}$, respectively.

At this stage, the first iteration is over. The modified ranges of F and P are used for calculating the resonance frequency in the next iteration. With the new range of F and P, by referring to Figure 6, the normalized operational frequency and consequently the possible range of the resonance frequency are modified to $0.9700 < \Omega_{op} < 0.9707$ and $619.1\,\text{MHz} < f_{res} < 619.6\,\text{MHz}$.

Note that the updated range of the resonance frequency is within the previously calculated range of the resonance frequency. In general,

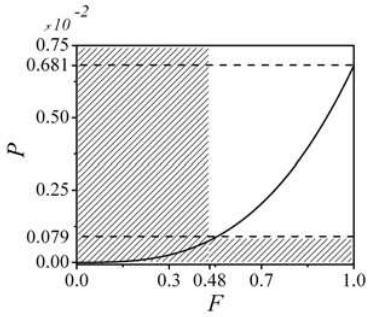

Figure 7. The banned area in Figure 5 introduced by inequality (19) has been cross-hashed. The white area is the permitted range for pairs of (F, P).

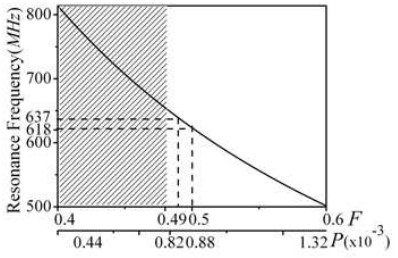

Figure 8. The graph shows the relation between the resonance frequency f_{res} (on vertical axes) and the geometrical factor, F (upper horizontal axes) and the physical factor, P (lower horizontal axes). The scale on F axes is linear, however, the scale on P axes is not linear.

it is not obvious that these two intervals overlap. There are three possible cases. Let $\mathcal{I}_i$ be the range of the resonance frequency calculated in the i-th iteration:

- Case 1: If $\mathcal{I}_i \subset \mathcal{I}_{i-1}$, then the new range of the resonance frequency is considered as $\mathcal{I}_i$.
- Case 2: If $\mathcal{I}_i \not\subset \mathcal{I}_{i-1}$ and $\mathcal{I}_{i-1} \cap \mathcal{I}_i \neq \emptyset$, the intersecting range would be considered as the valid range and it is renamed to $\mathcal{I}_i$.
- Case 3: If $\mathcal{I}_{i-1} \cap \mathcal{I}_i = \emptyset$, then no design will be obtained with the defined set of parameters. An option to provide a solution is to change the structural or fabrication parameters such as permeability of the host medium, the thickness of the conductor traces and the gap between traces.

In summary, after performing the second iteration, the values for the set $\{\Omega_{op}, F, P\}$ can be chosen from the following intervals:

$$\begin{cases} \Omega_{op} \in [0.9700, 0.9707] \\ F \in [0.4916, 0.5038] \\ P \in [8.209, 8.833] \times 10^{-4} \end{cases} \tag{22}$$

Note that any valid set of $\{\Omega_{op}, F, P\}$ from (22) specifies inclusions producing an AMM with $\mu_{\mathrm{Re}} = 9$ and $\tan\delta < 0.05$ at the operational frequency of $f_{op} = 600\,\mathrm{MHz}$.

Next, we check the tolerance of F and P to determine whether to terminate the iterations and go to the next step or to proceed to the third iteration and obtain narrower ranges. From (22), $\delta F/F = 2.45\%$ and $\delta P/P = 7.32\%$, both are larger than the fabrication tolerance declared in Table 1, thus requiring further iteration. Applying the third iteration, the lower and upper bound of the ranges of F and P become identical up to three significant digits. Therefore, F and P tolerances are smaller than the fabrication tolerance, and the iterations are terminated resulting in the following values (calculated up to three significant digits):

$$\begin{cases} \Omega_{op} \cong 0.970 \\ F \cong 0.503 \\ P \cong 8.88 \times 10^{-4} \\ f_{res} \cong 619.5 \times 10^{8} \end{cases} \tag{23}$$

Figure 9 shows the result of the second and the third iterations. Note that although the number of iterations depends on the desired accuracy of the design, inaccuracy in the circuit-based model and fabrication tolerances alter the characteristics of the fabricated AMM from the designed properties. Thus, it is sometimes preferable to run

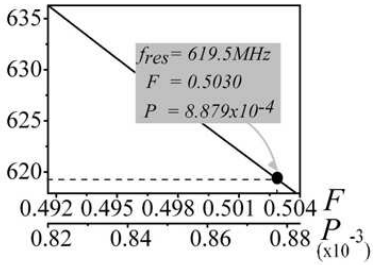

Figure 9. The graph shows the relation between the resonance frequency f_{res} (on vertical axes) and the geometrical factor, F, (upper horizontal axes) and the physical factor, P, (lower horizontal axes). Also, the calculated parameters in the third iteration marked in the graph.

Table 2. The output summary of the design.

freq (MHz)	μ_{Re}	$\tan\delta$
599	8.58	0.047
600	9.00	0.050
601	9.48	0.054

Step II one iteration less than the final iteration to have wider ranges for the design parameters (i.e., F, P and f_{res}).

Before continuing to the next step, we check if the calculated parameters are substituted in the model (Eq. (15)), the structure meets the design specifications. Based on the parameters calculated in (23), the permeability and MLT have been calculated over the requested bandwidth, and the results were summarized in Table 2. From Table 2, it can be seen that the requested frequency bandwidth of 2 MHz associated with a permeability deviation of about 10% is satisfied.

According to Table 2, the MLT at the upper frequency is about 9% above the requested threshold. This is due to the fact that in the design procedure (specifically when using (21) and (20)) the value of MLT is kept 0.050 at the operational frequency $f_{op} = 600$ MHz. As the MLT is a monotonically increasing function (in absolute value) before the resonance frequency, the MLT becomes less than 0.050 at the lower side of the frequency band, and becomes higher than 0.050 at the upper side of the frequency band. Because the slope of the MLT

function is not clear a priori, there are two possible ways to address this issue. First, the designer can perform the design procedure by choosing a random number smaller than the value declared for MLT in the Table 1. This method has the risk of choosing a number too small which might fail the design procedure or choosing a number not small enough resulting in MLT violating the desired criteria. The second option is to repeat the design procedure by subtracting the MLT at the operational frequency from the difference of the MLT at the upper side of the frequency band and the desired value of MLT. For instance, in the case study considered here, the adjusted value of MLT is 0.46. This option incurs the cost of repeating the procedure one more time but it confidently gives the proper result as the MLT function curves upward for frequencies closer to the resonance frequency, and it gives a safe side for the new design so that the new MLT at the upper side of the frequency band does not exceed the desired criteria.

4.4. Step IV — Perimeter and Area of the Inclusion

In this step, the area and the perimeter of inclusions are determined by using the geometrical factor and the resonance frequency calculated in Step III. From (10), the area of an inclusion is $s = FA$. Also, the perimeter and area of an inclusion are connected through the resonance frequency of the inclusion, i.e., $l = [\mathcal{Q}/2\pi f_{ref}]^2 s^{-1}$ (see (12)). Using these relations, the perimeter of the inclusion is plotted in Figure 10 versus its area over the calculated range of the resonance frequency given by (22).

Each point (*area*, *perimeter*) $= (s, l)$ of the curve in Figure 10 introduces a contour $\Gamma(s, l)$ with the perimeter of l and the area of s. The contour can accept any topology as long as it fits the pair (s, l).

Let $\mathcal{G}$ introduce the set (s, l) which is the outcome of the design procedure. From Figure 10, the end points of the sl-curve are:

$$(196.6\,\text{mm}^2, 64.56\,\text{mm}), (201.5\,\text{mm}^2, 66.79\,\text{mm}) \in \mathcal{G} \tag{24}$$

The point $P\,(201.2\,\text{mm}^2,\ 66.66\,\text{mm})$ corresponds to the selection in (23). In fact, an AMM composed of inclusion's topologies with the area and perimeter equal to $201.2\,\text{mm}^2$ and $66.66\,\text{mm}$, respectively, create an analytical magnetic response similar to what summarized in Table 2.

Despite the fact that the set $\mathcal{G}$ has been obtained from the physics of the problem, the pair (s, l) may or may not be fit in an actual geometrical shape. Based on Dido's isoperimetric problem [22], among all possible contours with the same surface area, the circle provides the minimum circumference. Hence, for a certain area s and perimeter l,

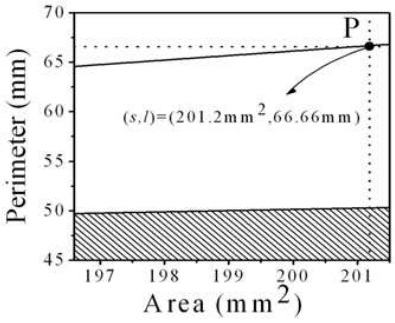

Figure 10. The graph shows the relation between s and l. The hashed region describes pairs of (s, l) which do not fit in any physically realized geometry.

an actual geometry satisfies Dido's inequality formulated as:

$$l \geq 2\sqrt{\pi s} \tag{25}$$

In Figure 10, the region corresponding to non-realizable geometries is cross-hashed. It can be seen from the figure that all inclusions introduced by the curve are realizable. In other words, no pair (s, l) of inclusions introduced in $\mathcal{G}$ will be eliminated by Dido's geometrical constraint. If the set of pairs (s, l) which satisfies Dido's inequality is denoted by $\mathcal{D}$, the outcome of the design procedure is $\mathcal{G} \cap \mathcal{D}$.

In General, there are three possibilities for a curve characterized by s and l according to Dido's inequality. These possibilities are:

- Case 1: If $\mathcal{G} \subset \mathcal{D}$, then $\mathcal{G}$ is the outcome of the design procedure.
- Case2: If $\mathcal{G}$ is not completely located in $\mathcal{D}$, then $\mathcal{G} \cap \mathcal{D}$ is the outcome of the design procedure.
- Case3: If $\mathcal{G} \cap \mathcal{D} = \emptyset$, the design procedure does not provide any inclusions geometry to meet the design objectives. An option to provide a solution is to change the structural or fabrication parameters such as permeability of the host medium, the thickness of the conductor traces and the gap between traces.

Note that, as $0 < F < 1$, from (10), we have $0 < s < A$. In other words, the maximum inclusion's area which can be determined through the design methodology is less than the unit cell area A. The inclusion's perimeter is only limited from below to $2\sqrt{\pi s}$ due to Dido's inequality, and it doesn't have an upper limit. Therefore, the inclusion's perimeter can be determined to any value through the design methodology.

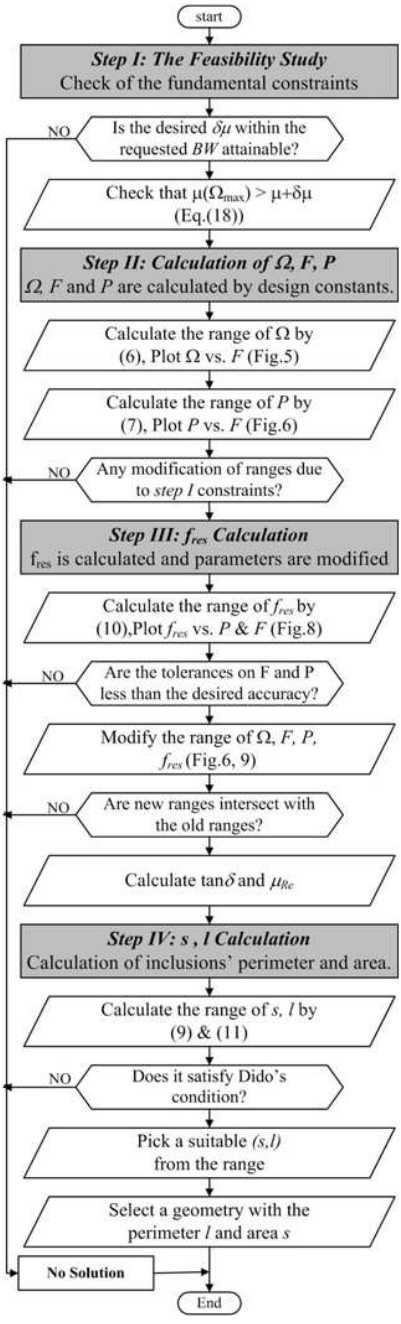

Figure 11. A flowchart as the design methodology.

Figure 11 summarizes the design steps in a flowchart. It can also be proved that the proposed routine converges. The details of this proof is out of the scope of this paper, and it is the subject of future publications.

5. APPLICATION

In this section, the proposed technique is applied to design a metamaterial structure with specific properties listed in Table 1 and the results are compared with three dimensional full wave simulations. According to the Design Data Sheet in Table 1, the area and perimeter of the corresponding AMM inclusions are equal $(s, l) = (201.2\,\text{mm}^2, 66.66\,\text{mm})$.

Split circular or square ring resonators are among the most common inclusions for constructing metamaterial media. The area and perimeter of a circle and a square are dependent. Thus, knowing the value of the area, the perimeter of the geometry is calculated and vice versa. Since the proposed technique has generated independent values for the perimeter and area of an inclusion of an AMM, common metamaterial inclusions proposed in the literature are not applicable. In [23], a Rose curve resonator was introduced with the following geometric parametrization:

$$R_n(r_0, a) : r(\theta) = r_0 + a\cos(n\theta) \tag{26}$$

where $r(\theta)$ represents the position of the contour in the xz-plane, and the angle θ sweeps the curve (aside from a small slit on the contour) and is measured from the x-axis. a is the amplitude of the sinusoidal function added to a circle with the radius r_0. The order of the Rose curve, n is a positive integer number which be chosen freely and which determines the number of crests and troughs along the circle's circumference. Therefore, the parameters $r(\theta)$ and a are strictly calculated such that the final curve has a certain area and perimeter. An example of a 5th order Rose curve is shown in Figure 12.

For this application, $(s, l) = (201.2\,\text{mm}^2, 66.66\,\text{mm})$. Therefore, r_0 and a are calculated for Rose curves of orders $n = 7, 8, 9$, (see Table 3).

The values in Tables 1 and 3 were used to set up an AMM based on Rose curve resonators in the commercial 3D full wave simulator HFSS. In the simulation setup, a periodic boundary condition is used to mimic an infinite three dimensional AMM structure. The permeability function was extracted from the S-parameters calculated using the full-wave simulation.

Figure 13 shows the analytically and numerically calculated permeability functions of media constructed using Rose curve

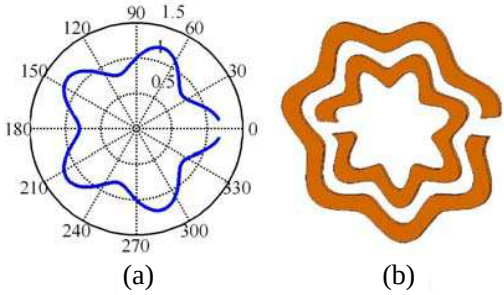

Figure 12. (a) A 5th order Rose curve with $r_0 = 1$, $a = 0.2$, (b) An edge-coupled inclusion designed using a 7th order Rose curve.

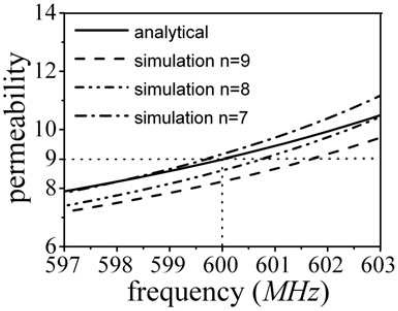

Figure 13. The dashed lines shows the simulated permeability function of the medium for n =7, 8 and 9. The solid line shows the analytically calculated permeability function of the medium for $n = 7, 8$ and 9. The plots of analytical solutions cannot be distinguished because they are identical.

Table 3. A set of candidates for Rose-curved inclusions.

n	r_0 (mm)	a (mm)	D (mm)
7	8.00	1.56	19.12
8	8.02	1.36	18.72
9	8.03	1.21	18.46

inclusions of orders $n = 7, 8$ and 9. The analytical response was generated using the proposed methodology and thus all the curves (for all the orders considered here) are expected to be identical because the

area and perimeter of inclusions with different orders were identical.

Note that the AMM is designed to work at the frequency of 600 MHz with 2 MHz bandwidth. Despite the fact that there is a slight shift in the resonance frequency or in the maximum magnitude of the permeability function, the graphs show a highly robust design satisfying the design criteria. For instance, for the case of $n = 7$, the numerical simulation yielded $\mu_{\mathrm{Re}} = 9 \pm 5.6\%$ at the frequency of 599.5 MHz with 2 MHz bandwidth. The shift in frequency from the desired magnetic property specified in Table 1 was about 0.08%. The achieved MLT is 0.048 which was also within the desired range.

6. CONCLUSION

A novel design methodology for artificial magnetic material with desired properties has been proposed based on analytical models introduced in earlier work. Analytical models show that the magnetic properties such as the real effective permeability, the magnetic tangent loss, and the flatness of the permeability function of the medium, all depend on the geometrical properties such as surface area and perimeter of the inclusion. We proposed a four-step iterative design methodology for design of AMMs. In the first step, the feasibility of the design is tested to meet the fundamental constraints. In consecutive steps, the geometrical and physical factors of the inclusion is synthesized, and finally the area and perimeter of the inclusion is calculated. An updated range of the inclusion's area and perimeter is obtained through consecutive iterations. Finally, if the outcome of the iterative procedure results in geometrical parameters that satisfy Dido's criterion, then a physical geometry exists meeting the design specifications. The methodology was applied to design of an AMM based on Rose curve resonators. The design technique was verified using numerical calculation based on a commercial simulator. The requested permeability function and corresponding designed structure are compared in a very good agreement.

APPENDIX A. THE PERMEABILITY MAXIMUM VALUE

The normalized frequency which maximizes the permeability function is calculated in terms of the geometrical and physical parameters. Correspondingly, a relationship for the maximum of the permeability function is derived.

From (6), the real part of the magnetic susceptibility can be

written as

$$\chi_{m\mathrm{Re}}(\Omega) = \chi_0(\Omega)(1+\xi(\Omega))^{-1} \tag{A1}$$

By limiting Ω to 0 and 1, we have

$$\lim_{\Omega\to 0} \chi_{mRe}(\Omega) \;=\; 0 \tag{A2}$$

$$\lim_{\Omega\to \infty} \chi_{m\mathrm{Re}}(\Omega) \;=\; 0 \tag{A3}$$

Therefore, because $\chi_{m\mathrm{Re}}(\Omega)$ is a positive function over the range of $\Omega \in [0,1]$, it is maximized at $\Omega_{\max} \in (0,1)$ which is the root of the first derivative of $\chi_{m\mathrm{Re}}(\Omega)$ over an interval (0, 1). Taking the derivative of $\chi_{m\mathrm{Re}}(\Omega)$ with respect to Ω,

$$\frac{1}{\chi_0}\frac{d\chi_0}{d\Omega} = \frac{1}{(1+\xi)}\frac{d\xi}{d\Omega} \tag{A4}$$

By substituting from (7), (8) and (9) in (A4), we have

$$\mathcal{B}^2 \cdot \Omega^3(1+\Omega^2) - (1-\Omega^2)^2 = 0 \tag{A5}$$

where $\mathcal{B} = \frac{P}{F^2}$. It is clear that the root of (A5) and equivalently the maximum of $\chi_{m\mathrm{Re}}$ approaches one if and only if $\frac{p^2}{F^4} \to 0$. In [11], it has been shown that for practical applications, $\frac{P^2}{F^4} \ll 1$. Hence, we can assume $\Omega_{\max} = 1-\alpha$ where $\alpha \ll 1$. Substituting $\Omega = 1-\alpha$ in (A5) and considering up to the second order of expansion, we obtain

$$(8-13\mathcal{B}^2)\alpha^2 + 8\mathcal{B}^2\alpha - 2\mathcal{B}^2 = 0 \tag{A6}$$

By solving (A6) for α, $\Omega_{\max}$ is obtained as

$$\Omega_{\max} = 1 - \frac{1}{2}\mathcal{B} + \frac{1}{2}\mathcal{B}^2 + \mathcal{O}(\mathcal{B}^3) \tag{A7}$$

and accordingly

$$\mathcal{M}ax(\chi_{mRe}) \simeq \frac{F}{2\mathcal{B}} - \frac{F}{8} + \frac{3F}{64}\mathcal{B} - \frac{43F}{256}\mathcal{B}^2 + \mathcal{O}(\mathcal{B}^3) \tag{A8}$$

For the maximum value of $F = 1$ and $\mathcal{B} = 0.1$ the error in the calculation of the maximum value of the magnetic susceptibility is less than 0.1%. In fact, even by taking only the first two terms in (A7) and (A8), the error remains less than 0.1%. After substituting $\mathcal{B} = \frac{P}{F^2}$, and considering the first two term in (A7) and (A8), the proof is completed.

Equivalently, for the permeability, we have

$$\mathcal{M}ax(\mu_{m\mathrm{Re}}) \simeq 1 - \frac{F}{8} + \frac{F^3}{2P} \tag{A9}$$

REFERENCES

1. Penury, J. B., A. J. Holden, D. J. Robbins, and W. J. Stewart, "Magnetism from conductors and enhanced nonlinear phenomena," *IEEE Transactions on Microwave Theory and Techniques*, Vol. 47, No. 11, 2075–2084, November 1999.
2. Marques, R., F. Medina, and R. Rafii-El-Idrissi, "Role of bianisotropy in negative permeability and left-handed metamaterials," *Physical Review B*, Vol. 65, No. 14, 144440, April 2002.
3. Maslovski, S., P. Ikonen, I. Kolmakov, and S. Tretyakov, "Artificial magnetic materials based on the new magnetic particle: Metasolenoid," *Progress In Electromagnetics Research*, Vol. 54, 61–81, 2005.
4. Baena, J. D., R. Marques, F. Medina, and J. Martel, "Artificial magnetic metamaterial design by using spiral resonators," *Physical Review B*, Vol. 69, No. 1, 141–145, January 2004.
5. Boybay, M. and O. M. Ramahi, "Near-field probes using double and single negative media," *Physical Review E*, Vol. 79, No. 1, 016602–016611, January 2009.
6. Ikonen, P. M. T., K. N. Rozanov, A. V. Osipov, P. Alitalo, and S. A. Tretyakov, "Magnetodielectric substrates in antenna miniaturization: Potential and limitations," *IEEE Transactions on Antennas and Propagation*, Vol. 54, No. 11, 391–3399, November 2006.
7. Pendry, J., "Negative refraction makes a perfect lens," *Physical Review Letters*, Vol. 85, No. 18, 3966–3969, 2000.
8. Landy, N. I., S. Sajuyigbe, J. J. Mock, D. R. Smith, and W. J. Padillal, "Perfect metamaterial absorber," *Physical Review Letters*, Vol. 100, No. 20, 207–402, May 2008.
9. Lahiri, B., A. Z. Khokhar, R. M. Delarue, S. G. McMeekin, and N. P. Johnson, "Asymmetric split ring resonators for optical sensing of organic materials," *Optics Express*, Vol. 4, No. 3, 1107–1115, January 2009.
10. Smith, D. R. and J. B. Pendry, "Homogenization of metamaterials by field averaging," *Journal of Optical Society America B*, Vol. 23, No. 3, 391–403, March 2006.
11. Kabiri, A., L. Yousefi, and O. M. Ramahi, "On the fundamental limitations of artificial magnetic materials," *IEEE Transactions on Antennas and Propagation*, Vol. 58, No. 7, 2345–2353, July 2010.
12. Sauviac, B., C. R. Siovski, and S. A. Tretyakov, "Double split-ring resonators: Analytical modeling and numerical simulation,"

Electromagnetics, Vol. 24, No. 5, 317–338, February 2004.

13. Shamonin, M., E. Shamonina, V. Kalinin, and L. Solymar, "Properties of a metamaterial element: Analytical solutions and numerical simulations for a singly split double ring," *Journal of Applied Physics*, Vol. 95, No. 57, 3778–3784, April 2004.
14. Ikonen, P. and S. A. Tretyakov, "Determination of generalized permeability function and field energy density in artificial magnetics using the equivalent-circuit method," *IEEE Transactions on Microwave Theory and Techniques*, Vol. 55, No. 1, 92–99, January 2007.
15. Baena, J. D., L. Jelinek, R. Marques, and M. Silveirinha, "Unified homogenization theory for magnetoinductive and electromagnetic waves in split-ring metamaterials," *Physical Review A*, Vol. 78, 013842(1)–013842(5), July 2008.
16. Markos, P. and C. Soukoulis, "Numerical studies of left-handed materials and arrays of split ring resonators," *Physical Review E*, Vol. 65, No. 3, 36622–36623, March 2002.
17. Marques, R., F. Mesa, J. Martel, and F. Medina, "Comparative analysis of edge- and broadside-coupled split ring resonators for metamaterial design — Theory and experiments," *IEEE Transactions on Antennas and Propagation*, Vol. 51, 2572–2581, October 2003.
18. Baena, J. D., L. Jelinek, and R. Marqus, "Towards a systematic design of isotropic bulk magnetic metamaterials using the cubic point groups of symmetry," *Physical Review B*, Vol. 76, 24515(1)–24515(14), December 2007.
19. Gay-Balmaz, P. and O. J. F. Martin, "Efficient isotropic magnetic resonators," *Applied Physics Letters*, Vol. 81, No. 5, 939–941, 2001.
20. Landau, L. D., L. P. Pitaevskii, and E. Lifshitz, *Electrodynamics of Continuous Media*, 2nd Edition, Pergamon Press, 2004.
21. Cummer, S. A., B.-I. Popa, and T. H. Hand, "Q-based design equations and loss limits for resonant metamaterials and experimental validation," *IEEE Transactions on Antennas and Propagation*, Vol. 56, No. 1, 127–132, January 2008.
22. Forray, M. J., *Variational Calculus in Science and Engineering*, McGraw Hill, 1968.
23. Kabiri, A. and O. M. Ramahi, "nth order rose curve as a generic candidate for RF artificial magnetic material," *Applied Physics Letters*, Vol. 103, 831–834, January 2011.